Spontaneously Sn Doped Bi/BiOx Core–shell Nanowires Toward High-Performance CO2 Electroreduction to Formate

Yang Zhao
Hunan University
Xunlin Liu
Hunan University
Zhixiao Liu
Hunan University
Xin Lin
Hunan University
Jiao Lan
College of Materials Science and Engineering, Hunan University
Yanlong Zhang
Hunan University
YR Lu
National Synchrotron Radiation Research Center
Ming Peng
Hunan University
Ting-Shan Chan
National Synchrotron Radiation Research Center https://orcid.org/0000-0001-5220-1611
Yongwen Tan (tanyw@hnu.edu.cn)
Hunan University https://orcid.org/0000-0003-1486-4048

Article

Keywords: electrochemical CO2 reduction, nanowires, CO2 conversion

Posted Date: March 9th, 2021

DOI: https://doi.org/10.21203/rs.3.rs-264108/v1

Spontaneously Sn Doped Bi/BiO_x Core–shell Nanowires Toward High-Performance CO_2 Electroreduction to Formate

Yang zhao[1], Xunlin Liu[2], Zhixiao Liu[2], Xin Lin[1], Jiao Lan[1], Yanlong Zhang[1], Ying-Rui Lu[3], Ming Peng[1], Ting-Shan Chan[3], Yongwen Tan[1]*

[1] *College of Materials Science and Engineering, State Key Laboratory of Advanced Design and Manufacturing for Vehicle Body, Hunan University, Changsha, Hunan 410082, China*

[2] *College of Materials Science and Engineering, Hunan University, Changsha, Hunan 410082, China*

[3] *National Synchrotron Radiation Research Center, Hsinchu 300, Taiwan*

Keywords: electrochemical dealloying, nanowires, carbon dioxide reduction, Bi-based alloy, core-shell structure

*Corresponding Author: tanyw@hnu.edu.cn

Electrochemical CO_2 reduction to formate using renewable electricity provides a promising strategy to product value-added carbon-based fuels and feedstocks. However, it still remains a grand challenge to further reduce the cathodic potentials and increase current density for the large-scale practical applications of formate. Herein, we report that spontaneously Sn doped Bi/BiO_x nanowires (denoted as Bi/Bi(Sn)O_x NWs) are prepared from electrochemical dealloying strategy. The Bi/Bi(Sn)O_x NWs exhibit impressive CO_2 electroreduction activity to formate with a Faradaic efficiency (FE) > 92% from -0.5 to -0.9 V versus reversible hydrogen electrode (RHE), and achieve a current density of 301.4 mA cm^{-2} at -1.0 V vs. RHE

under gas diffusion cell configuration. In-situ Raman spectroscopy and theory calculations reveal that the incorporation of Sn atoms into BiO_x species modulates the electron states of Bi, allowing the *OCHO intermediate to favorably adsorb onto the reconstructed $Bi(Sn)O_x$ surface while promotes formate generation by suppressing the competitive hydrogen evolution reaction. This work provides effective in-situ construction of the metal/metal oxide hybrid composites with heteroatom doping and offers insights in promoting practical CO_2 conversion technology.

Electrochemical reduction of CO_2 into value-added chemicals or fuels provieds a promising strategy to alleviate the excessive combustion of fossil fuels and greenhouse effects, especially driven by renewable energy[1, 2]. The nontoxic formate is an important liquid product of electrochemical CO_2 conversion, which has been widely applied to various energy and industrial fields, such as hydrogen storage and fuel cells[3-5]. However, the inevitable bottleneck in electrochemical CO_2 reduction reaction leads to the poor selectivity and low efficiency for the production of desired formate because of the large energy barrier required for activating CO_2 to *OCHO intermediate and the inevitably competing hydrogen evolution reaction (HER) in aqueous media[6]. Therefore, it is immensely significant yet challenging to exploit high-activity, selectivity, and stability catalysts for the large-scale practical formate applications.

Recently, various heterogeneous electrocatalysts including metals (such as Pd, Bi, In, Sn, etc.) and their derivatives have shown recent progress in electrochemical CO_2 reduction to formate[7-9]. Among them, Bi-based oxide nanostructures generally prefer

to convert CO_2 into formate due to their strong adsorption of CO_2 intermediates and poor activity for HER[10-13]. Unfortunately, various Bi-based oxides usually suffer from undesirable activity in a low and wide cathodic potential window owing to their relatively low intrinsic electrical conductivity and low selectivity toward formate production[14-16]. One feasible strategy for promoting electrical conductivity is to prepare core–shell nanostructured catalysts with a highly conductive metal core and thin metal oxide shell, which can potentially modulate the electronic properties and tune the binding strength of the intermediates[17-19]. To further promote the activity of electrocatalysts, engineering new Bi-based materials by incorporating other components has emerged as an efficient strategy to modulate the reactant adsorption, activation and product desorption, such as Bi_2O_3 nanosheets modified by nitrogen-doped graphene quantum dots or multi-channel carbon matrix [13,20], Sn-Bi eutectic alloys[21-23], hybrids of Sn nanosheets and Bi nanoparticles[24], Bi@Sn core–shell nanoparticles[17], which are promising candidates for the electrochemical reduction of CO_2 to formate. Obviously, the problems of low formate selectivity and high competition with hydrogen evolution at low overpotentials remain unsolved even by using flow cell reactors.

In this work, we present novel Sn doped Bi/BiO_x nanowires with high electrical conductivity Bi metallic core and amorphous Sn-doped BiO_x shell through electrochemical dealloying. The $Bi/Bi(Sn)O_x$ NWs exhibits an excellent catalytic activity and selectivity for electrochemical electrochemical CO_2 reduction to formate over a wide negative potential range, with a Faradaic efficiency (FE) > 92% from -0.5

to -0.9 V versus reversible hydrogen electrode (RHE), and a maximum FE value of 98 ± 2 % at −0.7 V under gas diffusion cell configuration. The impressive performance is attributable to the incorporation of Sn atoms into BiO_x species, which can modulate the electron states of Bi, allowing the *OCHO intermediate to favorably adsorb onto the $Bi(Sn)O_x$ surface while promotes formate production by suppressing the competitive hydrogen evolution reaction.

Results

Material synthesis and characterization. A schematic illustration of the fabrication process toward novel $Bi/Bi(Sn)O_x$ NWs is shown in **Figure 1a**. By utilizing the disparity in electrochemical stability of the Bi and Sn phases, the Sn atoms were priority dissolved from the arc-melt spinning Bi_1Sn_{99} (at%) alloy ribbons by galvanic corrosion in 0.25 M H_2SO_4 solution at the applied potential of -0.3 V versus Ag/AgCl (**Supplementary Fig. 1**)[25,26]. During the dealloying of the Bi-Sn alloys, as the Sn atoms are continuously dissolved into the electrolyte from the Sn phase, the Bi atoms would be released and reorganized into well-arranged single-phase Bi-based nanowires along the direction of etching (**Fig. 1b**)[27,28]. Scanning electron microscopy (SEM) image (**Fig. 1c**) displays the continuous nanowire structure of the etched ribbons. The corresponding energy dispersive X-ray spectroscopy (EDS) analysis provides a chemical composition of Bi/Sn atom ratio is ~95:5 (**Supplementary Fig. 2**). Aberration-corrected high-angle annular dark-field scanning transmission electron microscopy (HAADF-STEM) image clearly shows that crystalline range of $Bi/Bi(Sn)O_x$ NWs with

diameter of ~30 nm is surrounded by thick amorphous-like shells (**Fig. 1d**). The selected-area electron diffraction (SAED) exhibits a single diffraction pattern, which could be indexed as a rhombohedral Bi structure (JCPDS No. 44-1246) with a growth direction of [101] (**Fig.1e**). The lattice distance measured from fast Fourier transformation (FFT) of HAADF-STEM image (**Fig. 1f**) exhibits the interface of Bi (101) core and amorphous oxide shell. The distribution of different elements in the nanowires is revealed by STEM-EDS element maps (**Fig. 1g**), where Bi is homogeneously present in the central region, while coexistence of Bi, Sn and O on the surface of the metallic Bi core.

The chemical state and electronic structure of the Bi/Bi(Sn)O_x NWs were further investigated by X-ray photoelectron spectroscopy (XPS) and X-ray absorption spectroscopy (XAS) measurements. **Figure 2a–c** show Bi/Bi(Sn)O_x NWs survey spectra and typical XPS fitting curves of the Bi 4f, Sn 3d, and O 1s spectra before and after Ar^+ etching (5 keV, 3 min), along with the Bi_2O_3 and SnO_2 nanoparticles as references. The Bi 4f spectrum of the Bi/Bi(Sn)O_x NWs in **Figure 2a** could be deconvoluted into Bi^0 and Bi^{3+} components. This suggests that Bi^0 and Bi^{3+}species co-exist on the surfaces of Bi/Bi(Sn)O_x NWs. More importantly, the intensity of the Bi^0 peak was increased after the Ar^+ etching, which could be associated with the expose of the inner metallic Bi core while the decrease of the outer layer of oxide shell. Moreover, the Sn 3d XPS spectrum of Bi/Bi(Sn)O_x NWs dramatically decreases in intensity in the etched XPS spectra (**Fig. 2b**). The surface adsorbed oxide (531.8 eV) was also removed after the Ar^+ etch (**Fig. 2c**). Specifically, the surface compositions obtained from XPS

agree with the SEM-EDS results (**Supplementary Table 1**). The Bi L_3-edge X-ray absorption near edge structure (XANES) spectra of the Bi/Bi(Sn)O_x NWs in **Figure 2d** reveal visible similarities with that of the Bi and Bi_2O_3 reference. These similarities are to be expected, given that Sn atoms in both Bi_2O_3 and BiO_x lattices are expected to be octahedrally coordinated by oxygen atoms, leading to similarities in their structural and electronic properties. Meanwhile, the XANES spectra apparently reveal that Bi L_3-edge position of the Bi/Bi(Sn)O_x NWs is located between the Bi foil and Bi_2O_3, indicating coexistence of metallic Bi and oxidation state Bi species in the core-shell structure. The corresponding Fourier-transformed extended x-ray absorption fine structure (FT-EXAFS) spectra and inversed FT-EXAFS are presented in **Figure 2e, f**, respectively. The similar positions of the metallic Bi peak positions suggest that these bonds lengths in the Bi/Bi(Sn)O_x NWs are similar to those in the Bi reference, strongly indicating the metallic Bi-core structure. In stark contrast, the observed Bi–O peaks appear at distinctly positions in the Bi/Bi(Sn)O_x NWs spectra, revealing a distinct structural difference relative to the pure Bi reference. Interestingly, the formation of Bi_2O_3, SnO_2 can be predicted from the Bi–Sn–O ternary phase diagram at low Sn content (region iii, **Supplementary Fig. 3**)[23], which is consistent with our XPS and XAS results. According to the above-mentioned surface and bulk sensitive techniques, we can conclude that the prepared Bi-based nanowires display a core-shell structure with metallic Bi cores and amorphous Bi(Sn)O_x shells. In fact, the synergetic effect of the metallic core and the amorphous oxide shell in providing both good bulk conductivity and surface activity is beneficial to high performance CO_2 electroreduction.

Electrochemical CO_2 reduction performance. The electrocatalytic CO_2 reduction performance of the Bi/Bi(Sn)O_x NWs were evaluated in a gas diffusion flow cell with 1.0 M KOH electrolyte (**Supplementary Fig. 4**), along with commercial Bi, Bi_2O_3, and SnO_2 as references (**Supplementary Fig. 5, 6**). **Figure 3a** shows linear sweep voltammetry (LSV) curves of the Bi/Bi(Sn)O_x NWs with commercial Bi, Bi_2O_3, and SnO_2 nanopowder catalysts. The cathodic current density of the Bi/Bi(Sn)O_x NWs sharply increases and markedly reaches −301.4 mA cm^{-2} at −1.0 V vs. RHE under CO_2 flow, suggesting its superior CO_2 reduction activity. Resultant gaseous products were periodically sampled and examined using gas chromatography (GC), and the liquid products were analyzed by nuclear magnetic resonance (NMR) spectroscopy (**Supplementary Fig. 7**, **8**). Faradaic efficiency of Bi/Bi(Sn)O_x NWs and commercial Bi, Bi_2O_3, SnO_2 nanopowders were calculated and summarized in **Figure 3b and Supplementary Figure 9**. Bi/Bi(Sn)O_x NWs possess the highest selectivity towards formate, with above 92% Faradaic efficiency in a wide potential range (from −0.5 to −0.9 V) and a maximum FE of nearly 100% at – 0.7 V versus RHE (**Fig. 3c**). In contrast, Bi, Bi_2O_3, and SnO_2 catalysts show lower selectivity towards formate, while CO or H_2 dominates in the low potential range (**Supplementary Fig. 9**). In addition, the partial current density of formate on Bi/Bi(Sn)O_x NWs is significantly higher than that of commercial Bi, SnO_2, and Bi_2O_3 nanopowders (**Fig. 3d**), showing a desirable formate current density of ~100 mA cm^{-2} at a maximum formate FE of −0.7 V. Compared with reported Bi-based catalysts for electrochemical CO_2 reduction, Bi/Bi(Sn)O_x NWs maintain the highest formate selectivity over a wide potential range (**Supplementary**

Table 3). The energy efficiency (EE) of the Bi/Bi(Sn)O_x NWs is further evaluated, which shows a high EE over 60% in a wide potential range (**Supplementary Fig. 10**). Tafel analysis is indispensable for understanding the kinetics of CO_2 electroreduction. The Bi/Bi(Sn)O_x NWs exhibit a much lower Tafel slope of 124 mV dec^{-1}, suggesting that the chemical rate-determining step (RDS) is the first electron transfer step to generate surface adsorbed $CO_2^{\bullet-}$ species (**Supplementary Fig. 11**)[29-31]. Furthermore, the Bi/Bi(Sn)O_x NWs displays remarkably higher CO_2 adsorption capability compared with commercial Bi and Bi_2O_3 (**Supplementary Fig. 12**). This could lead to CO_2 enrichment on the local working electrode surface, which is beneficial for CO_2 activation and reduction[32,33]. Electrochemical impedance spectroscopy (EIS) analysis further verifies that the Bi/Bi(Sn)O_x NWs catalyst with metallic core-shell structure could generate small internal resistance and rapid charge transfer behavior for a low onset potential and fast CO_2 reduction reaction (CO_2RR) kinetics (**Supplementary Fig. 13**). To evaluate the intrinsic activity of the catalysts, we measured the electrochemically active surface area (ECSA) for Bi/Bi(Sn)O_x NWs, Bi, Bi_2O_3, and SnO_2 (**Supplementary Fig. 14**) and evaluated their ECSA-normalized partial current densities for formate production, hydrogen evolution, and CO production (**Supplementary Fig. 15**). Strikingly, Bi/Bi(Sn)O_x NWs show lower HER and CO production rates, which results in it having higher selectivity for formate production than pure Bi, Bi_2O_3, and SnO_2. These results confirm that the presence of metallic Bi core in the hybrid catalysts could decrease the energy barrier and facilitate the charge-transfer process from the electrode to the adsorbed CO_2, contributing to excellent

selectivity and ultrahigh current density. In addition, a long-term stability testing on the Bi/Bi(Sn)O_x NWs catalyst shows a negligible current decay and a steady FE of formate over 10 h at an operated potential of -0.7 V. Furthermore, no detectable compositions and morphology changes were observed on Bi/Bi(Sn)O_x NWs after the long-term operation, implying the superior structural stability (**Supplementary Fig. 16, 17**).

Active sites identification and mechanisms of CO_2RR. To survey the detailed structure of the Bi/Bi(Sn)O_x NWs surface during CO_2RR, in situ electrochemical Raman spectroscopy analysis was performed to identify the dynamic evolution of the Bi/Bi(Sn)O_x NWs surface (**Supplementary Fig. 18**). As **Figure 4a** shown, three typical Raman peaks at 97 cm^{-1}, 128 cm^{-1} and 314 cm^{-1} are presented under open circuit potential (OCP), which are assigned to the Bi-Bi and Bi-O stretching mode[34,35]. When the cathodic potential is gradually increasing from -0.4 V to −0.8 V vs. RHE in the CO_2-saturated electrolyte, the peaks of the Bi-O are still remained under the actual CO_2RR condition. It is worth noting that the scattering intensity of Bi-O peak weakens but preserves strength to some extent at -0.8 V vs. RHE, indicative of partial reduction of the Bi(Sn)O_x shell in the Bi/Bi(Sn)O_x NWs catalyst during CO_2RR. Nevertheless, the Bi−O structure can be reconstructed when the potential is removed, which in accordance with previous reports[14,31]. These results indicate that Bi-O structure is stable under the maximum formate Faradaic efficiency, while it was being partial reduced to metallic Bi at high overpotential.

To gain further insights into the CO_2RR activity and selectivity toward formate production on the reconstructed Bi/Bi(Sn)O_x NWs, density functional theory (DFT)

calculations were carried out to analyze the thermodynamic reaction process. The structural models for the DFT calculations were built based on a Bi_2O_3 layer deposited on the Bi surface according to the above structural identifications (**Supplementary Fig. 19**). The binding strength of *OCHO intermediates could be inferred from the position of the highest pelectronic states (E_p) and the charge density distribution. In **Figure 4b**, the E_p of Bi/Bi(Sn)O_x moves more closely to the Fermi level (E_f) and displays a stronger electronic interaction between *OCHO, which also consistent with the stronger electronic interaction between *OCHO and the substrate (**Fig. 4b, inset**). We also explored the reaction pathways for CO_2 reduction to HCOOH and HER. In **Figure 4c**. the Bi/Bi(Sn)O_x catalyst shows a lower energy barrier (ΔG) for *OCHO formation, which indicate that the doped of Sn atom can greatly stabilize *OCHO. In addition, the calculated Gibbs free energies for H_2 pathway on Bi/Bi(Sn)O_x (0.6 eV) surfaces is higher than that of Bi/BiO_x (0.32 eV), indicating the superior inhibition of HER. Hence, according to the above results, we speculate the possible mechanism of the CO_2RR processes in Bi/Bi(Sn)O_x surface, where the CO_2 molecules can been fast adsorption and proton-coupled electron transfer to form *OCHO intermediates. The incorporation of Sn atoms into Bi-O structure can facilitate the stabilizing *OCHO, and eventually accelerate the production of formate (**Fig. 4d**).

Conclusions

In summary, we demonstrated a facile route to synthesis the Bi/Bi(Sn)O_x NWs with a metallic Bi core and amorphous Sn-doped BiO_x shells by electrochemical

dealloying method. The resultant Bi/Bi(Sn)O_x NWs yielded excellent eletrochemical CO_2 reduction activity with FE over 92% at a wide potential range (-0.5 ~ -0.9 V vs. RHE) and a high current density (> 300 mA cm^{-2} at -1.0 V) in the gas diffusion cell. Moreover, Bi/Bi(Sn)O_x NWs showed stable current density and FE_{HCOOH} without significant decay during chronoamperometry test over 10 h. In-situ Raman and DFT calculations suggested that the incorporation of Sn atoms into BiO_x surfaces that stabilizes the *OCHO intermediate and suppresses the HER. The present work opens a new avenue to develop new core/shell catalysts with the desired control on reaction pathways and target products for highly efficient CO_2RR, but offers a facile and economic strategy to create new atom doped oxide catalysts reconstructed from bimetallic surfaces for boosting other chemical reactions.

Methods

Materials synthesis. The Bi_1Sn_{99} (at%) precursor alloy ribbon was prepared by arc melting and copper roller spinning technique under an argon atmosphere. The alloy ribbons with the dimensions of ~3 mm wide and 40 μm thick were cut into thin plates with dimensions of 5 mm wide and 20 mm long for the subsequent dealloying process. Bi/Bi(Sn)O_x NWs catalysts was fabricated by electrochemically etching the Bi_1Sn_{99} precursors in a 0.25 M H_2SO_4 solution configuration with a Ag/AgCl and graphite sheet as the reference and counter electrode, respectively. The selective Sn phase dissolution process was determined by the critical oxidation potentials of the Sn in Bi_1Sn_{99} alloy ribbon. In our experiments, Bi/Bi(Sn)O_x NWs was obtained at a dealloying voltage of -0.3 V (vs. Ag/AgCl) for 3000 s after the almost dissolution of the Sn. The dealloyed samples were rinsed by deionized water for more than three times still the solution became neutral. Commercial Bi (~200 mesh, 99.999%) was purchased from Alfa Aesar. Bismuth (III) oxide (Bi_2O_3, 99.999%), Stannic (Ⅳ) Oxide (SnO_2, 99%) were purchased from Adamas.

Characterizations: XRD patterns of the samples were taken by using a Bruker D8 Advance X-ray diffraction with Cu Kα radiation (λ=1.5418 Å). Microstructure and chemical composition were inspected with a MIR3 TESCAN SEM (at 10 kV and 5.5 mm work distance.) equipped with an Oxford energy dispersive X-ray spectroscopy. The TEM, HAADF-STEM and EDS mapping were taken by a JEM-ARM 200F with double spherical aberration (Cs) correctors for both the probe-forming and image-forming objective lenses at an accelerating voltage of 200 kV. The chemical state and

composition of the samples were characterized using X-ray photoelectron spectroscopy (XPS, AXIS SUPRA) with a Al Kα monochromatic. The CO_2 adsorption isotherms were measured by a Micromeritics ASAP2460. Raman spectra were obtained by Witec alpha300 R confocal Raman microscopes with He/Ne laser of λ = 532 nm and 20 mW. In-situ electrochemical/Raman spectra were achieved in a commercial Raman cell using 1 M KOH electrolyte and CO_2 is flowing at 5 mL min^{-1} under different applied potential. X-ray absorption spectra, including the X-ray absorption near-edge structure (XANES) and extended X-ray absorption fine structure (EXAFS), were obtained at the Bi L_3-edge at the beamline 01C1 (National Synchrotron Radiation Research Center: NSRRC, Hsinchu, Taiwan). All spectra were obtained in the fluorescence mode at room temperature. The spectra were normalized with respect to the edge height after subtracting the pre-edge and post-edge backgrounds using Athena software.

Electrochemical CO_2RR measurements: All CO_2 reduction experiments were performed in a commercial gas-diffusion flow cell separated by anion exchange membrane (Sustainion X37-50). The two compartments were each filled with ~35 mL of 1 M KOH electrolyte. A Pt foil and Hg/HgO (1M KOH) electrode were used as the counter electrode and reference electrode, respectively. Electrode potentials were converted to the reversible hydrogen electrode (RHE) reference scale using $E_{RHE} = E_{Hg/HgO} + 0.098\ V + 0.059 \times pH$. The linear sweep voltammetry (LSV) curves were recorded with a CHI-760E electrochemical workstation with a scan rate of 5 mV s^{-1}. For clarity, all LSV data were not corrected for a negligible ohmic drop. The chronoamperometry tests were conducted at each potential for 40 min. The long-term

stability measurement was operated at the potential of – 0.7 V versus RHE for 10 h. The current densities were normalized to the geometric surface area. CO_2 gas was delivered into the cathodic compartment at a rate of 10 ml/min and was routed into a gas chromatograph (Shimadu, GC-2010 Plus). The catalyst was sprayed on a gas diffusion layer of Sigracet 29 BC with a surface area of 1 cm^2, the eventually loading mass is ~1 mg cm^{-2}.

The gaseous products from CO_2 electroreduction were quantified by a gas chromatograph equipped with a flame ionization detector (FID) for CO and a thermal conductivity detector (TCD) for H_2 quantification. Before the FID, a methanizer is equipped for the detection of CO. High-purity Argon (99.999%) was used as the carrier gas. The Faradaic efficiency of each gas product was calculated by the equation:

$$\text{FE}\ (\%) = \frac{neF}{Q} \times 100\%$$

where e is the number of electrons transferred, F is Faraday constant, n is the mole fraction of the product, and Q is the total charge.

Liquid products were quantified on Bruker 400 MHz NMR spectrometer. Typically, 500 μl of collected catholyte exiting the reactor was mixed with 100 μl D_2O containing 20 ppm (m/m) dimethyl sulphoxide (≥ 99.9%; Alfa Aesar) as the internal standard. The faradic efficiency for HCOOH generation was calculated as follows:

$$\text{FE}_{HCOOH}\ (\%) = \frac{Q_{HCOOH}}{Q_{total}} \times 100\% = \frac{n_{HCOOH}eF}{I \times t} \times 100\%$$

where n (mol) is the generated amount of formate; e (= 2) is the number of transferred electrons for 1 mol of formate generation; and t (s) is the electrolysis time.

The cathode energy efficiency was calculated to define the energy utilization

toward the HCOOH product using the following formula:

$$EE=\frac{1.23-E_{HCOOH}}{1.23-E_{applied}}\times FE_{HCOOH}\times 100\%$$

where E_{HCOOH} = -0.2 V vs. RHE is the thermodynamic potential for HCOOH formation, 1.23 V is the thermodynamic potential for the oxygen evolution reaction, and $E_{applied}$ is the applied potential vs. RHE[14].

DFT Calculations. The calculations were performed with the VASP package[36], using Perdew-Burke-Ernzerhof (PBE) of exchange correlation energy functional based on a generalized gradient approximation (GGA) method[37,38]. After testing the energy cutoff and k-points convergence, we chose 450 eV as our cutoff energy, and used a 5 × 5 × 1 k-points grid to sample the unit cell Brillouin zone[39]. The convergence thresholds were set as 1×10^{-5} eV/atom for the energy, and atomic relaxation was performed until all components of the residual forces were less than 0.02 eV/Å. The spin polarization is considered for magnetic atoms in all simulations and DFT-D3 correction is used to deal with van der Waals interactions. a Bi_2O_3 layer is deposited on two layer Bi (111) substrate as Bi/BiO_x model. For $Bi/Bi(Sn)O_x$ simulation, we adopted Sn replace the partial Bi atom in Bi_2O_3.

The Gibbs free energy of formation (ΔG) for each step is calculated by the following formula :

$$\Delta G=\Delta DFT+\Delta ZPE-T\Delta S$$

Where ΔDFT , ΔZPE and $T\Delta S$ are DFT energy change, the zero-point energy change and entropy change between the product and reactant, and temperature T is set as 298.15 K.

The D-band center calculation is based on J. K. Nørskov's works and uses the following formula[40]:

$$\Delta\varepsilon_d = \frac{\int_{-\infty}^{+\infty} x\rho(x)dx}{\int_{-\infty}^{+\infty} \rho(x)\,dx}$$

Where $\int_{-\infty}^{+\infty} x\rho(x)dx$ is the integral of the product of the energy level and the density of states from negative infinity to positive infinity and $\int_{-\infty}^{+\infty} \rho(x)\,dx$ is the integral of the density of states from negative infinity to positive.

References

1 De Luna, P. *et al.* What would it take for renewably powered electrosynthesis to displace petrochemical processes? *Science* **364**, eaav3506 (2019).

2 Shih, C. F. *et al*. Powering the future with liquid sunshine. *Joule* **2**, 1925-1949 (2018).

3 Han, N. *et al.* Promises of main group metal–based nanostructured materials for electrochemical CO_2 reduction to formate. *Adv. Energy Mater.* **10**, 1902338 (2019).

4 Lu, X. *et al.* Electrochemical reduction of carbon dioxide to formic acid. *ChemElectroChem* **1**, 836-849 (2014).

5 Xia, C. *et al.* Continuous production of pure liquid fuel solutions via electrocatalytic CO_2 reduction using solid-electrolyte devices. *Nat. Energy* **4**, 776–785 (2019).

6 Feaster, J. T. *et al.* Understanding selectivity for the electrochemical reduction of carbon dioxide to formic acid and carbon monoxide on metal electrodes. *ACS Catal.* **7**, 4822-4827 (2017).

7 Han, N. *et al.* Ultrathin bismuth nanosheets from in situ topotactic transformation for selective electrocatalytic CO_2 reduction to formate. *Nat. Commun.* **9**, 1320 (2018).

8 Lee, C. W. *et al.* Cyclic two-step electrolysis for stable electrochemical conversion of carbon dioxide to formate. *Nat. Commun.* **10**, 3919 (2019).

9 Wang, P. *et al.* Phase and structure engineering of copper tin heterostructures for efficient electrochemical carbon dioxide reduction. *Nat. Commun.* **9**, 4933 (2018).

10 Gong, Q. *et al.* Structural defects on converted bismuth oxide nanotubes enable highly active electrocatalysis of carbon dioxide reduction. *Nat. Commun.* **10**, 2807 (2019).

11 Tran-Phu, T. *et al.* Nanostructured β-Bi_2O_3 fractals on carbon fibers for highly selective CO_2 electroreduction to formate. *Adv. Funct. Mater.* **30**, 1906478 (2019).

12 Deng, P. *et al.* Metal-organic framework-derived carbon nanorods encapsulating bismuth oxides for rapid and selective CO_2 electroreduction to formate. *Angew. Chem. Int. Ed.* **59**, 10807-10813 (2020).

13 Liu, S. B. *et al*. Bi_2O_3 Nanosheets grown on multi-channel carbon matrix to catalyze efficient CO_2 electroreduction to HCOOH. *Angew. Chem. Int. Ed.* **58**, 13828-13833 (2019).

14 Yang, J. *et al.* Bi-Based Metal-organic framework derived leafy bismuth nanosheets for carbon dioxide electroreduction. *Adv. Energy Mater.* **10**, 2001709 (2020).

15 Garcia de Arquer, F. P. *et al.* 2D metal oxyhalide-derived catalysts for efficient CO_2 electroreduction. *Adv. Mater.* **30**, e1802858 (2018).

16 Yang, Q. *et al.* Novel Bi-doped amorphous SnO_x nanoshells for efficient electrochemical CO_2 reduction into formate at low overpotentials. *Adv. Mater.* **32**, 2002822 (2020).

17 Xing, Y. *et al.* Bi@Sn core–shell structure with compressive strain boosts the electroreduction of CO_2 into formic acid. *Adv. Sci.* **7**, 1902989 (2020).

18 Ye, K. *et al.* In situ reconstruction of hierarchical Sn-Cu/SnO_x core/shell catalyst for high-performance CO_2 electroreduction. *Angew. Chem. Int. Ed.* **59**, 4814 – 4821 (2020).

19 Das, S. *et al.* Core-shell structured catalysts for thermocatalytic, photocatalytic, and electrocatalytic conversion of CO_2. *Chem. Soc. Rev.* **49**, 2937-3004 (2020).

20 Chen, Z. *et al*. Nitrogen-doped graphene quantum dots enhance the activity of Bi_2O_3 nanosheets for electrochemical reduction of CO_2 in a wide negative potential region. *Angew. Chem. Int. Ed.* **57**, 12790 –12794 (2018).

21 Allioux, F. M. *et al.* Bi-Sn catalytic foam governed by nanometallurgy of liquid metals. *Nano Lett.* **20**, 4403-4409 (2020).

22 Yuan, T. *et al.* Two-dimensional amorphous SnO_x from liquid metal: mass production, phase transfer, and electrocatalytic CO_2 reduction toward formic acid. *Nano Lett.* **20**, 2916-2922 (2020).

23 Tang, J. *et al.* Advantages of eutectic alloys for creating catalysts in the realm of nanotechnology-enabled metallurgy. *Nat. Commun.* **10**, 4645 (2019).

24 Wen, G. B. *et al.* Orbital interactions in Bi-Sn bimetallic electrocatalysts for highly selective electrochemical CO_2 reduction toward formate production. *Adv. Energy Mater.* **8**, 1802427 (2018).

25 Zhao, Y. et al. 3D nanoporous iridium-based alloy microwires for efficient oxygen evolution in acidic media. Nano Energy **59**, 146-153 (2019).

26 Tan, Y. W. et al. 3D Nanoporous metal phosphides toward high-efficiency electrochemical hydrogen production. Adv. Mater. **28**, 2951-2955 (2016).

27 Wu, Q. et al. Identifying electrocatalytic sites of the nanoporous copper–ruthenium alloy for hydrogen evolution reaction in alkaline electrolyte. ACS Energy Lett. **5**, 192-199 (2020).

28 Erlebacher J, Aziz M J, Karma A & Dimitrov, N. Evolution of nanoporosity in dealloying. Nature **410**, 450-453 (2001).

29 Gao, S. *et al.* Partially oxidized atomic cobalt layers for carbon dioxide electroreduction to liquid fuel. *Nature* **529**, 68-71 (2016).

30 Zhang, J. *et al*. Oxygen vacancies in amorphous InO_x nanoribbons enhance CO_2 adsorption and activation for CO_2 electroreduction. *Angew. Chem. Int. Ed.* **58**, 5609-5613 (2019).

31 Deng, P. *et al.* Bismuth oxides with enhanced bismuth-oxygen structure for efficient electrochemical reduction of carbon dioxide to formate. *ACS Catal.* **10**, 743-750 (2019).

32 Lei, F. *et al.* Metallic tin quantum sheets confined in graphene toward high-efficiency carbon dioxide electroreduction. *Nat. Commun.* **7**, 12697 (2016).

33 Liu, S. *et al.* Efficient electrochemical reduction of CO_2 to HCOOH over Sub-2nm SnO_2 quantum wires with exposed grain boundaries. *Angew. Chem. Int. Ed.* **58**, 8499-8503 (2019).

34 Kim, S. *et al.* Shape-controlled bismuth nanoflakes as highly selective catalysts for electrochemical carbon dioxide reduction to formate. *Nano Energy* **39**, 44-52 (2017).

35 Pang, R. C. *et al.* Tracking structural evolution: operando regenerative CeO_x/Bi interface structure for high-performance CO_2 electroreduction. *Natl. Sci. Rev.* **7**, nwaa187 (2020).

36 Kresse, G. & Furthmüller, J. Efficiency of ab-initio total energy calculations for metals and semiconductors using a plane-wave basis set. *Comp. Mater. Sci.* **6**, 15-50 (1996).

37 Kresse, G. & Joubert, D. From ultrasoft pseudopotentials to the projector augmented-wave method. *Phys. Rev. B* **59**, 1758-1775 (1999).

38 Hammer, B., Hansen, L. B. & Norskov, J. K. Improved adsorption energetics within density-functional theory using revised Perdew-Burke-Ernzerhof functionals. *Phys. Rev. B* **59**, 7413-7421 (1999).

39 Monkhorst, H. J. & Pack, J. D. Special points for Brillouin-zone integrations. *Phys. Rev. B* **13**, 5188-5192 (1976).

40 Hammer, B. & Nørskov, J. K. Theoretical surface science and catalysis-calculations and concepts. *Adv. Catal.* **45**, 71-129 (2000).

Data availability. The data that support the findings of this study are available from the corresponding authors upon reasonable request.

Acknowledgments: The authors gratefully acknowledge financial support by the National Natural Science Foundation of China (Grant No. 51771072), the Youth 1000 Talent Program of China, the Outstanding Youth Scientist Foundation of Hunan Province (Grant No. 2020JJ2006), Fundamental Research Funds for the Central Universities, and Hunan University State Key Laboratory of Advanced Design and Manufacturing for Vehicle Body Independent Research Project (No. 71860007).

Author contributions: Y. W. T. conceived and supervised this study. Y. Z., X. L. J. Lan, and Y. Zhang carried out materials fabrication, characterizations, and electrochemical measurements. X. L. L. and Z. X. L performed the DFT calculations and computational models. Y. Z., M. P., Y. R. L., T. S. C. contributed to the XAS measurements and analyses of the XAS experiments results. Y. W. T. and Y. Z. wrote the paper. All authors contributed to discussions and manuscript review.

Competing financial interests: The authors declare no competing financial interests.

Figure Legends

Figure 1. Structural characterizations of Bi/Bi(Sn)O_x nanowires. (**a**) Schematic illustration for the preparation of the Bi/Bi(Sn)O_x NWs. (**b**) XRD patterns, (**c**) SEM image. (**d**) STEM-HAADF image. (**e, f**) Corresponding SAED pattern and enlarge image. (**g**) STEM-EDS element mapping of Bi, Sn, and O. Scale bars: (c) 1 μm, (d) 10 nm, (e) 5 1/nm, (f) 2 nm, (g) 20 nm.

Figure 2. **X-ray photoelectron spectroscopy and X-ray absorption spectroscopy characterizations of Bi/Bi(Sn)O_x NWs.** (**a**) Bi 4f, (**b**) Sn 3d, and (**c**) O 1s XPS spectra of the Bi/Bi(Sn)Ox NWs before and after Ar^+ etching. (**d**) Bi L_3-edge XANES spectra of the Bi/Bi(Sn)Ox NWs, Bi_2O_3, and Bi foil. (**e, f**) Corresponding FT-EXAFS and inversed FT-EXAFS spectra.

Figure 3. Electrochemical CO_2 reduction performance of Bi/Bi(Sn)O_x NWs in a flow cell. (**a**) LSV curves of the Bi/Bi(Sn)O_x NWs, Bi, Bi_2O_3, and SnO_2 catalysts in Ar- or CO_2-saturated 1.0 M KOH aqueous solution. (**b**) H_2, CO, and formate FEs of the Bi/Bi(Sn)O_x NWs. (**c, d**) Potential-dependent FE (c) and partial current density (d) of Bi/Bi(Sn)O_x NWs, Bi, Bi_2O_3, and SnO_2. (**e**) Long-term stability test of the Bi/Bi(Sn)O_x NWs at −0.7 V vs. RHE.

Figure 4. **In-situ Raman and DFT calculations.** (**a**) In-situ electrochemical Raman spectra of Bi/Bi(Sn)O_x NWs. (**b**) Projected p-orbital DOS of the Bi site with *OCHO

adsorbate, insert is charge density differences calculations of *OCHO bonded to Bi/BiO_x and $Bi/Bi(Sn)O_x$. (**c**) Free-energy diagrams for HCOOH, and H_2 formation on Bi/BiO_x and $Bi/Bi(Sn)O_x$. (**d**) The schematic illustration of CO_2 reduction processes on the $Bi/Bi(Sn)O_x$.

Figure 1.

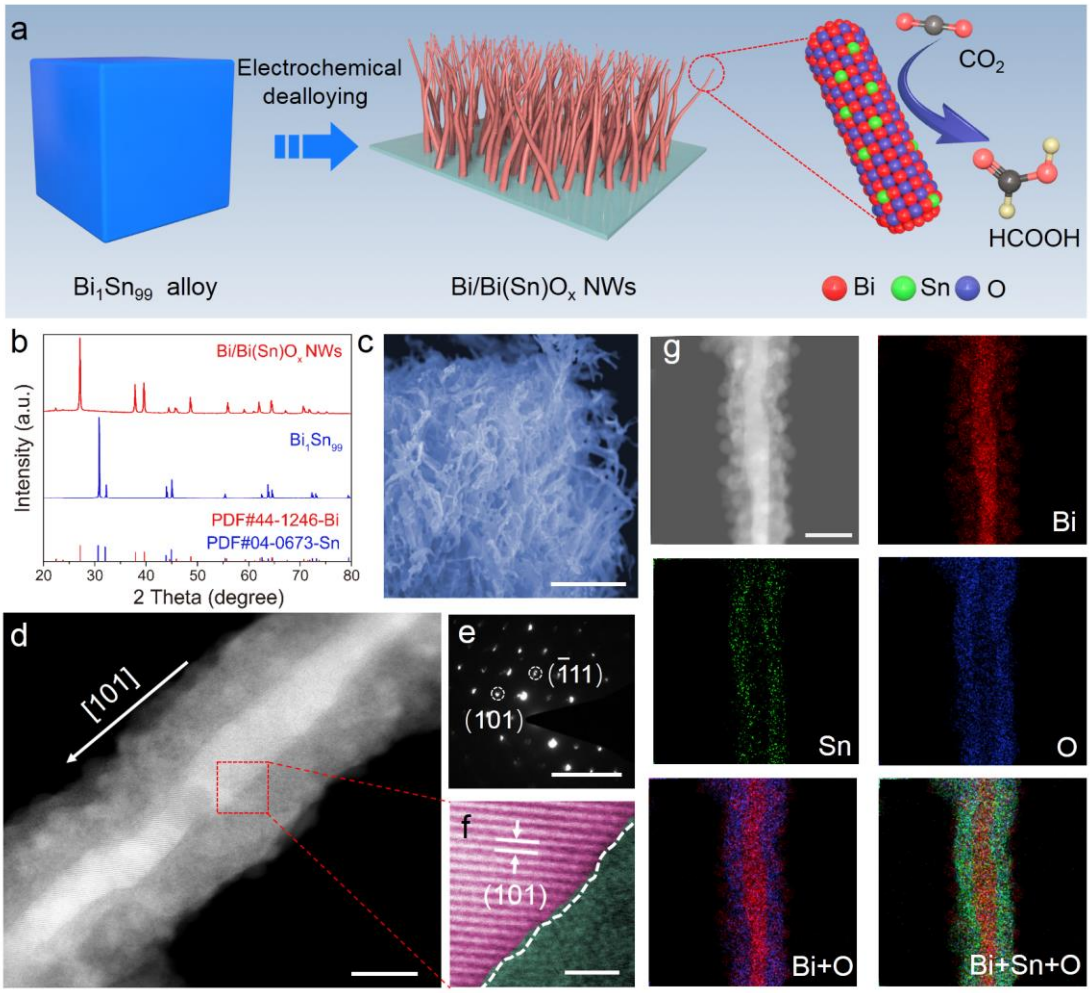
a
Electrochemical dealloying
CO_2
HCOOH
Bi_1Sn_{99} alloy
Bi/Bi(Sn)O_x NWs
Bi
Sn
O
b
Bi/Bi(Sn)O_x NWs
Bi_1Sn_{99}
PDF#44-1246-Bi
PDF#04-0673-Sn
Intensity (a.u.)
2 Theta (degree)
c
d
[101]
e
(111)
(101)
f
(101)
g
Bi
Sn
O
Bi+O
Bi+Sn+O

Figure 2.

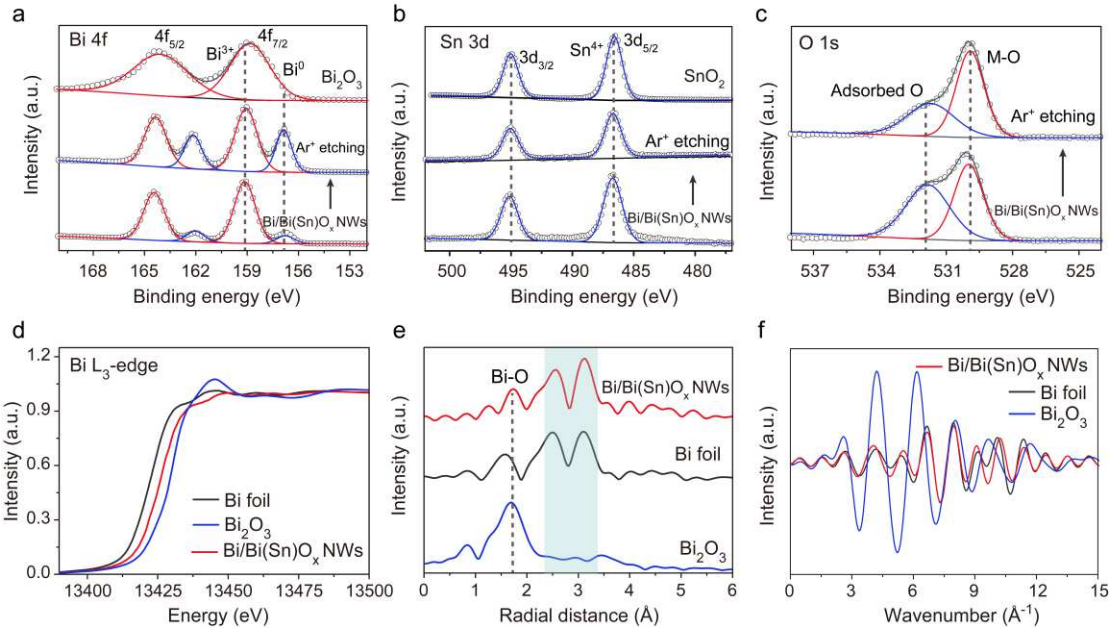
a
Bi 4f
4f5/2
Bi3+
4f7/2
Bi0
Bi2O3
Ar+ etching
Bi/Bi(Sn)Ox NWs
Intensity (a.u.)
168 165 162 159 156 153
Binding energy (eV)
b
Sn 3d
3d3/2
Sn4+
3d5/2
SnO2
Ar+ etching
Bi/Bi(Sn)Ox NWs
Intensity (a.u.)
500 495 490 485 480
Binding energy (eV)
c
O 1s
M-O
Adsorbed O
Ar+ etching
Bi/Bi(Sn)Ox NWs
Intensity (a.u.)
537 534 531 528 525
Binding energy (eV)
d
Bi L3-edge
Bi foil
Bi2O3
Bi/Bi(Sn)Ox NWs
Intensity (a.u.)
1.2 0.9 0.6 0.3 0.0
13400 13425 13450 13475 13500
Energy (eV)
e
Bi-O
Bi/Bi(Sn)Ox NWs
Bi foil
Bi2O3
Intensity (a.u.)
0 1 2 3 4 5 6
Radial distance (Å)
f
Bi/Bi(Sn)Ox NWs
Bi foil
Bi2O3
Intensity (a.u.)
0 3 6 9 12 15
Wavenumber (Å-1)

Figure 3.

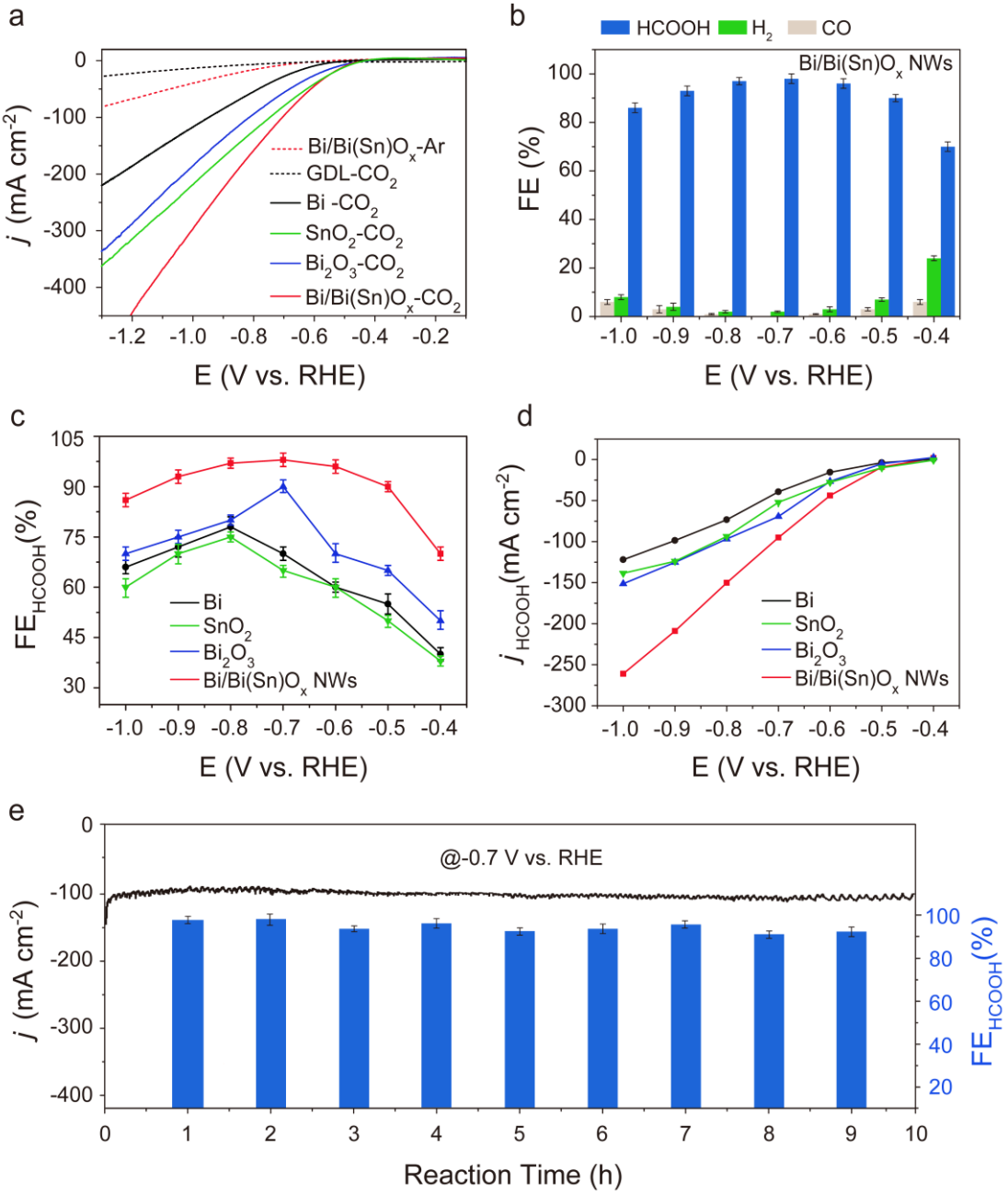
a
j (mA cm-2)
E (V vs. RHE)
Bi/Bi(Sn)Ox-Ar
GDL-CO2
Bi -CO2
SnO2-CO2
Bi2O3-CO2
Bi/Bi(Sn)Ox-CO2
b
HCOOH
H2
CO
Bi/Bi(Sn)Ox NWs
FE (%)
E (V vs. RHE)
c
FEHCOOH(%)
Bi
SnO2
Bi2O3
Bi/Bi(Sn)Ox NWs
E (V vs. RHE)
d
jHCOOH(mA cm-2)
Bi
SnO2
Bi2O3
Bi/Bi(Sn)Ox NWs
E (V vs. RHE)
e
@-0.7 V vs. RHE
j (mA cm-2)
FEHCOOH(%)
Reaction Time (h)

Figure 4.

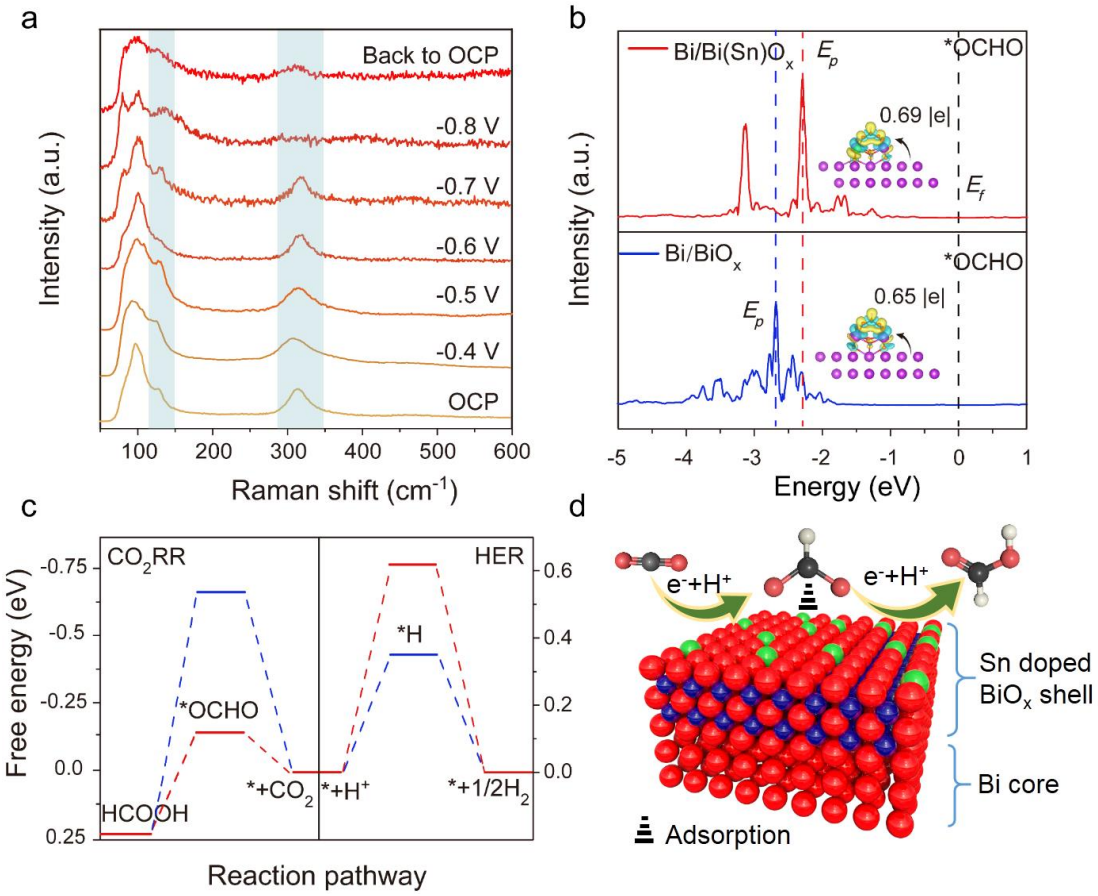
a
Back to OCP
-0.8 V
-0.7 V
-0.6 V
-0.5 V
-0.4 V
OCP
Intensity (a.u.)
100
200
300
400
500
600
Raman shift (cm-1)
b
Bi/Bi(Sn)Ox
Ep
*OCHO
0.69 |e|
Ef
Bi/BiOx
*OCHO
Ep
0.65 |e|
Intensity (a.u.)
-5
-4
-3
-2
-1
0
1
Energy (eV)
c
CO2RR
HER
-0.75
-0.5
-0.25
0.0
0.25
0.6
0.4
0.2
0.0
Free energy (eV)
*OCHO
*H
HCOOH
*+CO2
*+H+
*+1/2H2
Reaction pathway
d
e-+H+
e-+H+
Sn doped
BiOx shell
Bi core
Adsorption

Figures

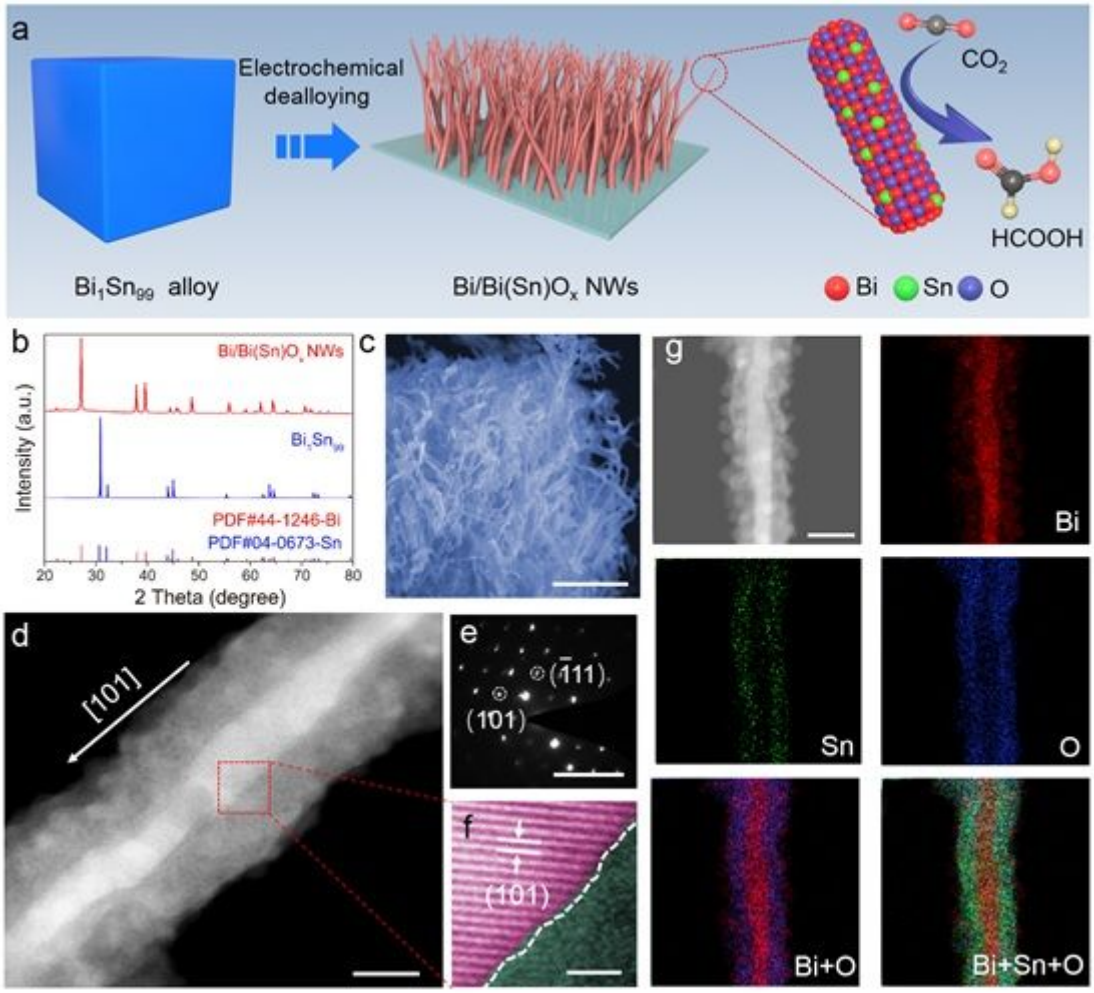

Figure 1

Structural characterizations of Bi/Bi(Sn)Ox nanowires. (a) Schematic illustration for the preparation of the Bi/Bi(Sn)Ox NWs. (b) XRD patterns, (c) SEM image. (d) STEM-HAADF image. (e, f) Corresponding SAED pattern and enlarge image. (g) STEM-EDS element mapping of Bi, Sn, and O. Scale bars: (c) 1 μm, (d) 10 nm, (e) 5 1/nm, (f) 2 nm, (g) 20 nm.

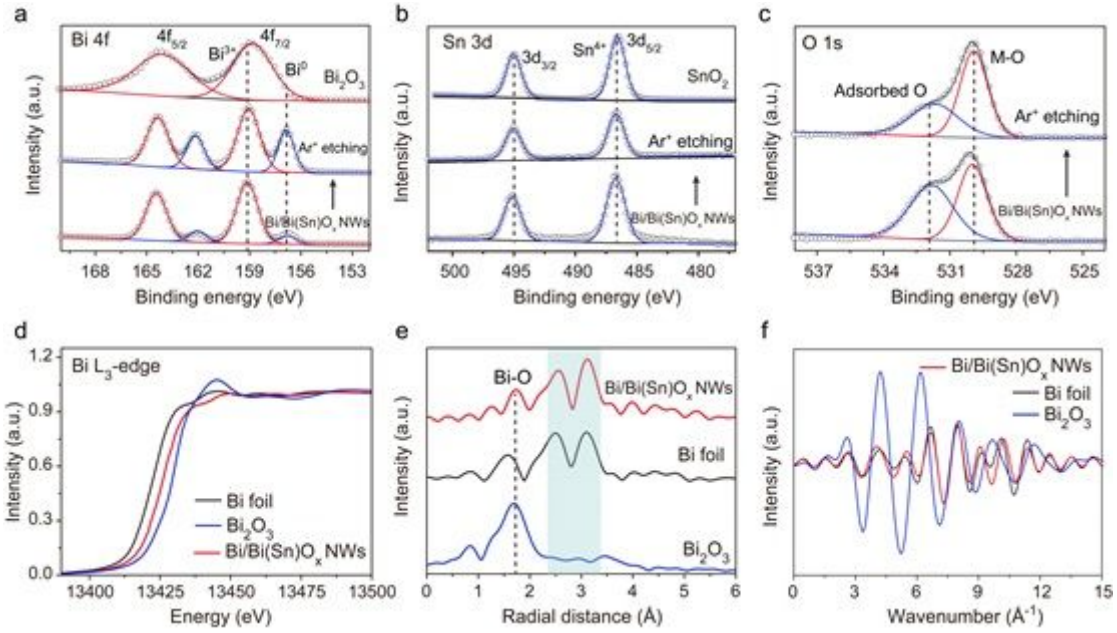

Figure 2

X-ray photoelectron spectroscopy and X-ray absorption spectroscopy characterizations of Bi/Bi(Sn)Ox NWs. (a) Bi 4f, (b) Sn 3d, and (c) O 1s XPS spectra of the Bi/Bi(Sn)Ox NWs before and after Ar+ etching. (d) Bi L3-edge XANES spectra of the Bi/Bi(Sn)Ox NWs, Bi2O3, and Bi foil. (e, f) Corresponding FT-EXAFS and inversed FT-EXAFS spectra.

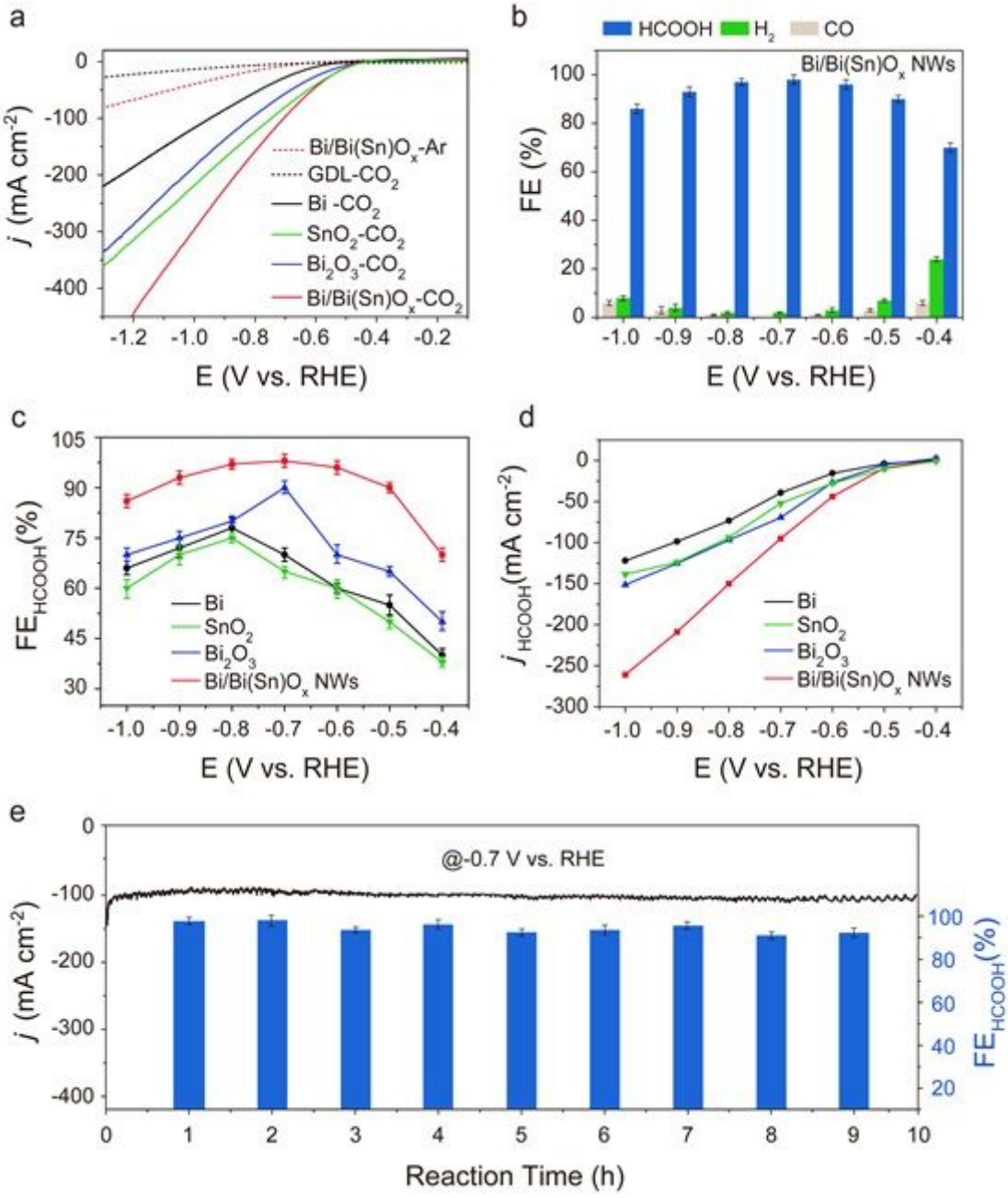

Figure 3

Electrochemical CO2 reduction performance of Bi/Bi(Sn)Ox NWs in a flow cell. (a) LSV curves of the Bi/Bi(Sn)Ox NWs, Bi, Bi2O3, and SnO2 catalysts in Ar- or CO2-saturated 1.0 M KOH aqueous solution. (b) H2, CO, and formate FEs of the Bi/Bi(Sn)Ox NWs. (c, d) Potential-dependent FE (c) and partial current density (d) of Bi/Bi(Sn)Ox NWs, Bi, Bi2O3, and SnO2. (e) Long-term stability test of the Bi/Bi(Sn)Ox NWs at −0.7 V vs. RHE.

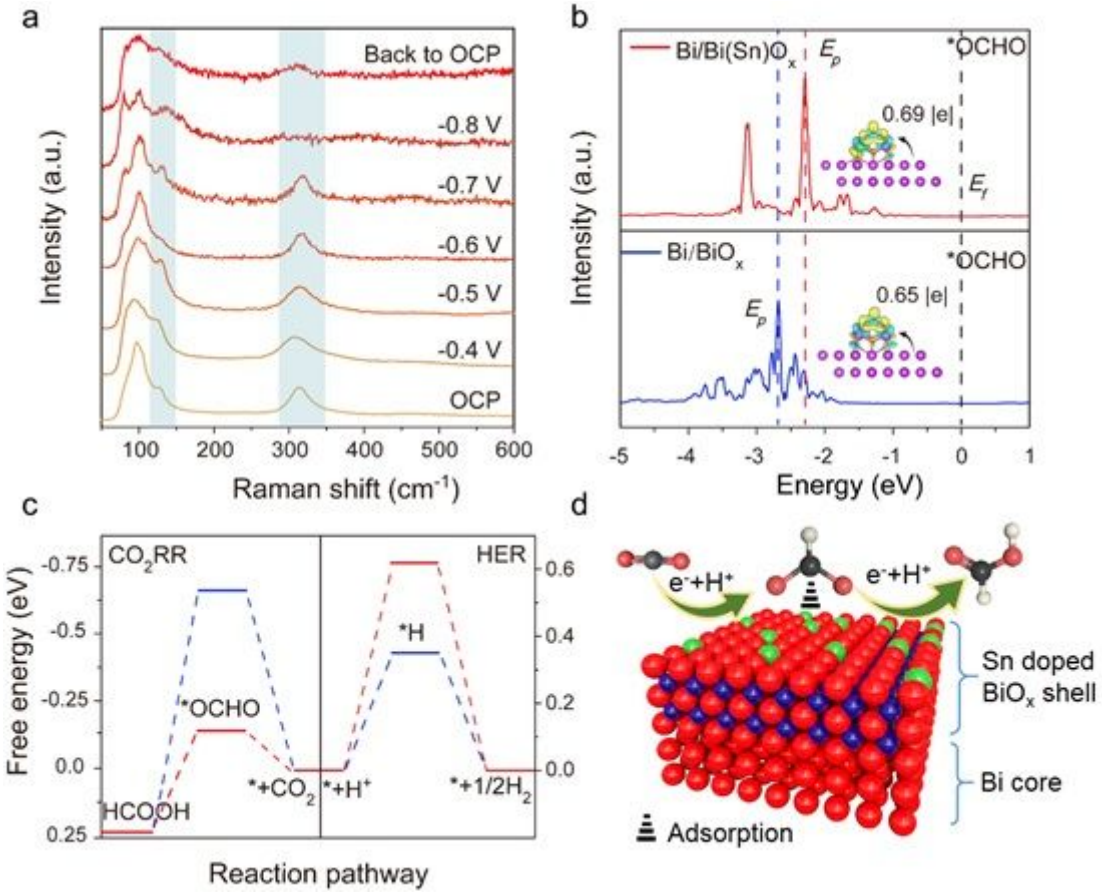

Figure 4

In-situ Raman and DFT calculations. (a) In-situ electrochemical Raman spectra of Bi/Bi(Sn)Ox NWs. (b) Projected p-orbital DOS of the Bi site with *OCHO adsorbate, insert is charge density differences calculations of *OCHO bonded to Bi/BiOx and Bi/Bi(Sn)Ox. (c) Free-energy diagrams for HCOOH, and H2 formation on Bi/BiOx and Bi/Bi(Sn)Ox. (d) The schematic illustration of CO2 reduction processes on the Bi/Bi(Sn)Ox.

Supplementary Files

This is a list of supplementary files associated with this preprint. Click to download.

- BibasedSI.docx